

Tunable Hyperuniformity in Cellular Structures

Yiwen Tang,¹ Xinzhi Li,² and Dapeng Bi^{1,*}

¹*Department of Physics, Northeastern University, Boston, MA 02115, USA*

³*Center for Theoretical Biological Physics, Northeastern University, Boston, Massachusetts 02215, USA*

²*Department of Physics, Carnegie Mellon University, Pittsburgh, PA 15213, USA*

Hyperuniform materials, characterized by their suppressed density fluctuations and vanishing structure factors as the wave number approaches zero, represent a unique state of matter that straddles the boundary between order and randomness. These materials exhibit exceptional optical, mechanical, and acoustic properties, making them of great interest in materials science and engineering. Traditional methods for creating hyperuniform structures, including collective-coordinate optimization and centroidal Voronoi tessellations, have primarily been computational and face challenges in capturing the complexity of naturally occurring systems. This study introduces a comprehensive theoretical framework to generate hyperuniform structures inspired by the collective organization of biological cells within an epithelial tissue layer. By adjusting parameters such as cell elasticity and interfacial tension, we explore a spectrum of hyperuniform states from fluid to rigid, each exhibiting distinct mechanical properties and types of density fluctuations. Our results not only advance the understanding of hyperuniformity in biological tissues but also demonstrate the potential of these materials to inform the design of novel materials with tailored properties.

INTRODUCTION

Density fluctuations provide vital thermodynamic and structural insights in many-particle systems [1–4]. While solids typically exhibit crystalline order with long-range density correlations, liquids lack such structured patterns. However, this distinction becomes blurred when considering amorphous materials, especially hyperuniform materials, which defy traditional categorizations by lacking crystalline structures. Hyperuniform materials are uniquely characterized by their suppressed density fluctuations over large scale [5–7], a property that enables them to blend order with randomness effectively. The anomalous suppression of these fluctuations is quantitatively manifested as the vanishing structure factor when the wave number q approaches zero, $\lim_{q \rightarrow 0} S(q) = 0$ [5]. This remarkable feature positions hyperuniform materials between ordered and disordered states, endowing them with unique optical [8–11], mechanical [12–15], and acoustic properties [16, 17], thereby opening new avenues in material science and engineering.

In previous studies, hyperuniform structures have been primarily generated through artificial computational methods, such as collective-coordinate energy optimization schemes [18–21] and "centroidal Voronoi tessellations" [7, 22]. While the former utilizes artificial multi-body potential functions in a reciprocal-space approach, the latter operates through a more direct real-space method aligning the centroids of cells with their generating points. However, both methods face challenges in simulating realistic or naturally occurring systems.

Given their intrinsic geometric properties, biological cellular structures emerge as natural candidates for exploring hyperuniformity. These structures are often amorphous, existing in both rigid and fluid states, and display a quasi-regular pattern that suggests an underlying order akin to hyperuniform materials [23–31]. Research into these natural systems has begun to reveal that hyperuniformity could serve as a new

metric to categorize the disorder within tissues [10, 32], with certain living tissues demonstrating true hyperuniform properties [33, 34]. Despite growing interest, there remains a significant gap in a comprehensive framework to systematically examine hyperuniformity in biological tissues. Recent studies employing vertex models have pinpointed hyperuniform ground states, highlighting the need for a deeper understanding of how individual cellular properties contribute to hyperuniformity and its correlation with the mechanical properties of tissues [10, 32].

In this work, we propose a complete framework for generating hyperuniform structures through the utilization of a theoretical model that describes the collective organization of cells in dense biological tissue. A broad spectrum of hyperuniform systems is observed, exhibiting diverse degrees of stealthiness [35] and short-range order. These hyperuniform structures can be fine-tuned by adjusting single-cell parameters, which encode the elasticity of the actin-myosin subcellular cortex and interfacial tension. Our work also reveals that the absence of cortex elasticity results in hyperuniform structures that exhibit a unique type of density fluctuations. We further characterize the mechanical properties of our hyperuniform structures, identifying hyperuniform fluid and hyperuniform rigid states.

MODEL

Epithelial cells, when densely packed into a monolayer, form a space-filling polygonal tiling. The geometric organization of this tiling is shaped by the mechanics of cell-cell interactions and the cells' interactions with their environment, effectively tuning the degrees of both short and long-range orders within the tissue. This makes the cellular structures excellent candidates for studying hyperuniformity.

In computational studies, vertex-based models have been extensively employed to analyze 2D tissue monolayers

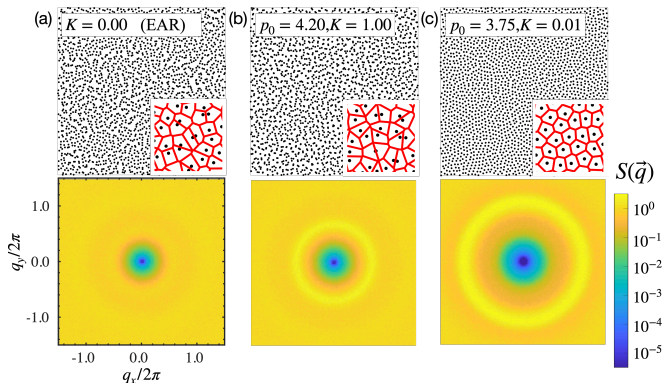


FIG. 1. **Hyperuniformity in a biological cellular structure.** Snapshots (top) for (a) EAR-packing, (b) hyperuniform fluid state, and (c) hyperuniform rigid state and their corresponding structure factor (bottom). The insets depict a magnified view of cell centers and their Voronoi tessellations.

and have shown remarkable agreements with experimental data [25, 29, 36, 37]. One such model, the Self-Propelled Voronoi (SPV) [26], utilizes Voronoi tessellation [38, 39] based on the cell centers $\{\vec{r}_i\}$ to define cell shapes and the connective topology of the cellular network. This approach provides a robust framework for exploring the emergent properties of cellular patterns and their potential for hyperuniform order. The non-dimensionalized form of the tissue’s mechanical energy is given by

$$\epsilon = \sum_{i=1}^N [(a_i - 1)^2 + K(p_i - p_0)^2], \quad (1)$$

where a_i and p_i denote the associated rescaled cell area and perimeter, respectively. In this formulation, the preferred area is set to be 1. In Eq. (1), the term quadratic in cell areas results from cell incompressibility and the monolayer’s resistance to height fluctuations [36, 40–42]. The term for cell perimeters arises from the contractility of the cell cortex. The perimeter elasticity K reflects relative contributions to the energy functional attributed to deviations from the preferred values of the respective geometrical components [36]. Our simulation (see Methods) mainly explores two key parameters, the perimeter elasticity K and effective target shape index p_0 [43]. The mechanically stable states of the SPV model are achieved via fast inertial relaxation engine (FIRE) algorithm [44, 45] under periodic boundary conditions.

RESULTS

Equal-Area Random (EAR) Packings The original definition of hyperuniformity, which refers to suppressed density [5, 46] or **equivalently, area fluctuations**, inspires a minimal way to achieve hyperuniformity in the model tissue collective: *enforcing uniform cell areas in the polygonal tiling*. This corresponds to setting $K = 0$ in Eq. (1). When the system

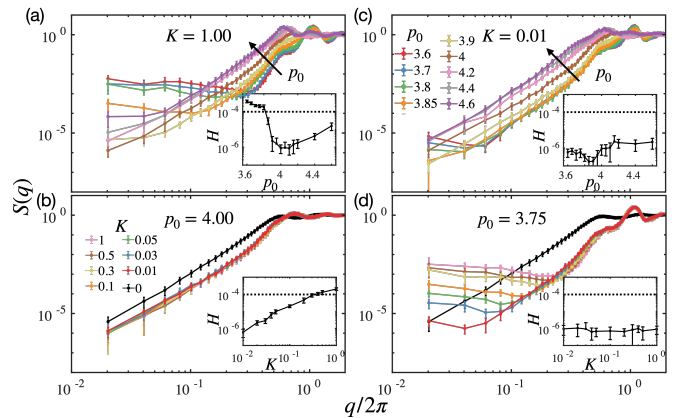


FIG. 2. **Structure factor $S(q)$ and hyperuniformity index H .** $S(q)$ as a function of $q/2\pi$ for $N = 2430$ under various conditions: (a) high cell perimeter constrain: fixed $K = 1.00$ with varying p_0 , (b) fluid phase: fixed $p_0 = 4.00$ with varying K , (c) low cell perimeter constrain: fixed $K = 0.01$ with varying p_0 , (d) rigid phase: fixed $p_0 = 3.75$ with varying K . The insets are H as the function of (a,c) p_0 and (b,d) K . The black dashed lines represent the empirical threshold of 10^{-4} commonly used to denote hyperuniformity in a finite system.

reaches the ground state (i.e. $\epsilon = 0$), it is by definition hyperuniform. Furthermore, these ground states are highly degenerate and simply connected [26], resulting in an ensemble of random structures. We refer to these as Equal-Area Random packings or EAR packings. An example is shown in Fig. 1(a) along with the ensemble-averaged structure factor $S(\vec{q})$ (see Methods), which diminishes to values below 10^{-5} near $\vec{q} = 0$. EAR packings are strictly hyperuniform [47, 48], evidenced by the continuous decrease of $S(q)$ as q diminishes without reaching saturation, $S(q) \sim q^4$ (SI Fig. S1(a)). EAR packing is a simple yet powerful way to generate hyperuniformity that has not been considered so far. In the following section, we will systematically explore the diverse classes of hyperuniform states achievable by manipulating K and p_0 . Throughout our work, EAR packing serves as a baseline for comparison with other hyperuniform structures.

Hyperuniform Fluid State In vertex-based models, extensive research has demonstrated that the target shape index p_0 governs a mechanical phase transition between solid and liquid states of tissue—solid when $p_0 < p_0^*$ and liquid for $p_0 > p_0^*$ [43, 49]. Further studies indicate potential hyperuniformity in the liquid phase [10, 32]. However, these investigations were constrained by limited system sizes [10] and provided inconclusive results regarding whether the liquid phase is consistently hyperuniform or only exhibits hyperuniformity at specific values of p_0 [32]. Therefore, we next undertake a systematic examination of how hyperuniformity might manifest across different phases of the SPV model

While maintaining a constant perimeter elasticity of $K = 1$, we explored target shape index $p_0 \in [3.60, 4.60]$, spanning across the critical rigidity point at $p_0^* \approx 3.813$ [49], which includes both solid and fluid states. The structure factor $S(q)$ for these p_0 values shows suppressed density fluctuations as

$q \rightarrow 0$, as confirmed in Fig. 2(a). Using the hyperuniformity index H (see methods), we observed that the solid phase ($p_0 < p_0^*$) exhibits non-hyperuniformity, with H values typically above 10^{-4} . At p_0^* , H sharply drops to around 10^{-6} , indicating consistent hyperuniformity in the fluid phase. Additionally, $S(q)$ displays a plateau at low q values, becoming more pronounced with larger system sizes, as illustrated in SI Fig.S1(b). Despite the real-space similarities between the hyperuniform fluid (Fig.1(b)) and EAR packings, the fluid states exhibit a distinct ‘stealthy’ hyperuniformity [35] (detailed in Methods), further differentiated from EAR packings by variations in K , as shown in Fig.2(b).

Hyperuniform Rigid State EAR-packing is only constrained by cell area and is inherently hyperuniform. However, the introduction of constraints on cell perimeters counteracts the hyperuniformity in the rigid phase, as shown in Fig. 2(a). This prompts the question: Can we tilt the balance in favor of the cell area constraint, thereby fostering hyperuniformity in the rigid phase? Fig. 2(c) suggests that a reduction in K could achieve it, giving $H \ll 10^{-4}$. Therefore, it is clear that hyperuniformity can hold for both *fluid and rigid* structures. A representative example of a hyperuniform rigid state is shown in Fig. 1(c). It possesses $S(\vec{q} \rightarrow 0)$ values below 10^{-5} but displays unique configurations and peaks in structure factor, which distinguishes it from EAR-packing and hyperuniform fluid states. Fig. 2(d) illustrates how K affects the structure factor of a solid state at fixed $p_0 = 3.75$. Decreasing K shifts the low- q plateau in $S(q)$ downwards. Consequently, the hyperuniformity index H descends below a threshold 10^{-4} corresponding to hyperuniformity, despite being in the rigid state. This suggests that the hyperuniformity is significantly influenced by the perimeter elasticity K and it does not always coincide with rigid or fluid behavior which is fully characterized by the shear and bulk moduli (SI Fig. S2). Therefore, hyperuniformity and rigidity can be independently tuned. Additionally, the low- q plateau of $S(q)$ makes it ‘stealthy’ (see [35] and Methods). The upper bound of the plateau, denoted as q_{th} is related to the stealthiness parameter χ via $\chi \propto 1/q_{th}$ in the thermodynamic limit (see Methods). Therefore, decreasing K decreases χ , as shown in SI Fig. S3. We further show that q_{th} is independent of the system size and initial conditions (SI Fig. S1(d) and Fig. S4). The dependence of q_{th} on K is not confined to the rigid phase but also observed in the fluid phase, as demonstrated in larger system sizes when comparing SI Fig. S1(b) and (c).

Short-Range Order In addition to long-range order, the model tissue can possess a large variation of short-range order. We compute the pair correlation function (see Methods) for varying different values of p_0 at $K = 1$ (Fig. 3(a)). For the solid phase ($p_0 < 3.81$), there is strong mutual exclusion between nearest neighbors due to effective short-range repulsion [26], therefore suppressing $g(r)$ at short distances up to the first peak $r \approx 1.1$ (The packing of regular hexagons with a unit area has a nearest-neighbor distance of approximately $r_{nn} = 2\sqrt{\frac{1}{2\sqrt{3}}} \approx 1.075$). At longer distances, the peaks of

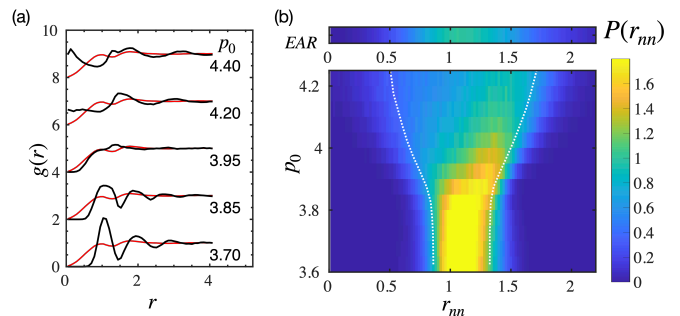


FIG. 3. **Increased p_0 weakens the short-range order.** (a) Pair-correlation function $g(r)$ at different values of p_0 . The results have been shifted for clarity. The red line represents $g(r)$ in EAR-packing ($K = 0$) for comparison. (b) The probability density function of the distance between neighboring cells r_{nn} for different p_0 and EAR-packing. The dashed lines indicate the mean of nearby and distant adjacent cells.

$g(r)$ decay rapidly, similar to a liquid [50]. In the fluid phase ($p_0 > 3.81$), the peaks of $g(r)$ broaden and become increasingly indistinguishable at higher p_0 's. There is also a lack of neighbor-neighbor exclusion as the cells no longer interact via purely repulsive interactions [26]. Deeper into the fluid regime ($p_0 > 4.20$), cells can become arbitrarily close. Consequently, the peak approaching $r = 0$ arises, leading to a loss of short-range order in the system. Here the short-range order resembles that of a gas rather than a fluid.

As the $g(r)$ is a distance-based metric, it does not provide sufficient information on the short-range order when its peaks become indistinguishable. We therefore also analyze a topology-based metric, $P(r_{nn})$, which is the distribution of distances between adjacent cells (Fig. 3(b)). In the solid phase, $P(r_{nn})$ shows a narrow peak centered at around $r \approx 1.1$, which simply corresponds to the first peak in the $g(r)$. However, in the fluid phase, as p_0 is increased, $P(r_{nn})$ broadens significantly and its mean increases. Here, cells become more elongated to accommodate the high target perimeters, thus widening the range of distances between neighboring cells. When two neighboring elongated cells align, their centers are brought closer together, whereas in the non-aligned case, the centers are further apart. These two types of cell neighbor pairs can be demonstrated by looking at the distance between nearest adjacent cells vs furthest adjacent cells shown as dotted white lines in Fig. 3(b). The short-range analysis is done at $K = 1$, but the observations hold true for all finite values of K . Despite the dramatic change induced by K in the long-range order $S(q)$, the short-range order remains unaffected by the choice of a finite K (see SI Fig. S5). With that said, however, the EAR-packing ($K = 0$) exhibits a unique $g(r)$ and $P(r_{nn})$ (Fig. 3).

Cell Shape Distributions In the preceding sections, we have investigated the long-range and short-range orders on the tissue scale, and distinct the EAR-packings from hyperuniform fluid states. What is the underlying mechanism of different hyperuniformities from a perspective of cell level? Here

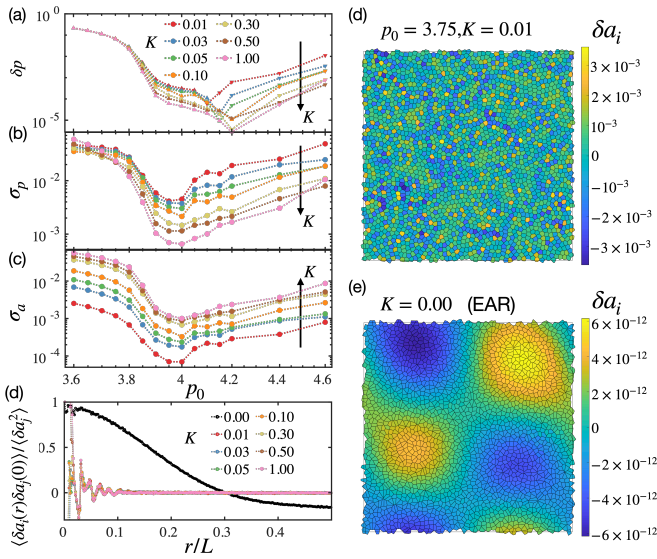


FIG. 4. **The distribution of cell perimeters and areas** (a) The deviation from the target shape index, denoted as $\delta p = \langle p_i - p_0 \rangle$, (b) the standard deviation of cell perimeters p_i , and (c) the standard deviation of cell areas a_i , are examined across various values of K as functions of the target shape index p_0 . (d) The area correlation as the function of r for EAR Packing ($K = 0.00$) vs that for stealth hyperuniformity ($K \neq 0.00, p_0 = 3.75$). The represented tissue snapshot of (e) stealth hyperuniformity ($p_0 = 3.75, K = 0.01$) and (f) EAR packing ($K = 0.00$) are colored by $\delta a_i = a_i - \langle a_i \rangle$.

we characterize the distribution of cell perimeters and areas at various K and p_0 values shown in Fig. 4. In the rigid phase ($p_0 < 3.81$), the average cell perimeters $\langle p_i \rangle$ hover around 3.81[26], resulting in significant deviations $\delta p = \langle p_i - p_0 \rangle \sim 0.01$. At $K = 1$, the large deviations δp in the rigid phase dominate the energy equation Eq. (1), which can be rewritten as $\langle \epsilon \rangle / N = \sigma_a^2 + K\delta_p^2 + K\sigma_p^2$. The minimization focusing on the p term weakens the constraint on the area term, causing a relatively high value for σ_a , thus excluding hyperuniformity. Conversely, in the fluid state, $\langle p_i \rangle$ demonstrates a linear growth pattern with p_0 , keeping $\delta p < 0.01$. Hyperuniform fluid state occurs even when $K = 1$. The logarithmic scale of δp reveals a valley located within the range of [4.10, 4.20].

Decreased K corresponds to weaker perimeter control, having higher deviation δp and larger fluctuation σ_p , while exerting stronger control over the cell area, resulting in smaller fluctuation σ_a . The fundamental characteristic underlying hyperuniformity lies in the standard deviation of cell area σ_a , which positively correlates with H , as shown in SI Fig. S6.

Both σ_p and σ_a reach minima at $p_0 \approx 4$, which slightly deviates from the average cell perimeter $\langle p_i \rangle = 4.08$ observed in EAR Packing. This discrepancy could potentially be attributed to the asymmetric distribution of p_i compared to the Gaussian constraint in finite K .

As shown in Fig. 4(e) and (f), the distribution of cell areas could be distinct between stealth hyperuniformity and EAR packing. To characterize the property, we calculate the area correlation function which is defined as $\langle \delta a_i(r) \delta a_j(0) \rangle / \langle \delta a_i^2 \rangle$,

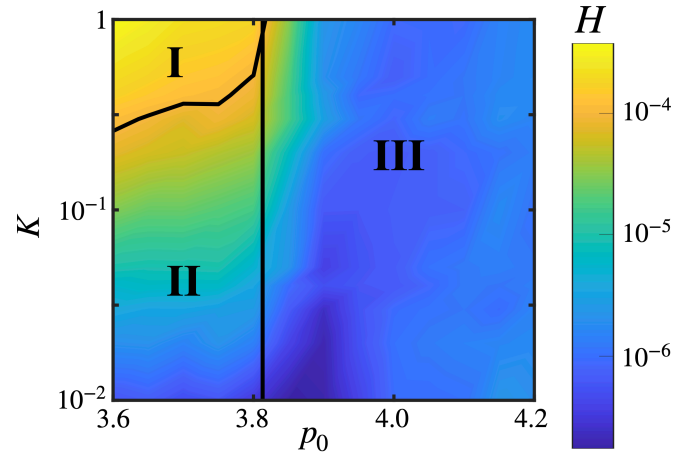


FIG. 5. **Phase diagram of hyperuniformity index H as a function of target shape index p_0 and perimeter modulus K .** It encompasses three distinctive phases: (I) non-hyperuniform rigid state, (II) hyperuniform rigid state, and (III) hyperuniform fluid state.

where $\delta a_i = a_i - \langle a_i \rangle$. We find that most EAR-packing states have long-range area correlation (solid black line in Fig. 4(d)), indicating a unique pattern where areas $A > 1$ and $A < 1$ are distinctly clustered and well-separated (Fig. 4(f)). Conversely, for $K > 0$ (Fig. 4(e)), the intermixing of areas $A > 1$ and $A < 1$ depicts a discrete pattern.

A phase diagram linking hyperuniformity and mechanics

The properties of hyperuniformity and rigidity define three different phases quantified by the hyperuniformity index and elastic modulus. The results are summarized by a phase diagram in Fig. 5. In the rigid regime $p_0 < 3.81$, tissues are all rigid but exhibit transition from hyperuniformity to non-hyperuniformity with increasing of K . In the fluid regime $p_0 > 3.81$, tissues are all fluid and hyperuniform. Notably, the existence of a fluid non-hyperuniform phase within current parameter ranges hinges on the chosen criterion value for hyperuniformity, which is empirical.

DISCUSSION

Our study introduces a new approach for creating hyperuniform structures in biological tissues, leveraging biologically inspired interactions instead of traditional artificial computational methods. We extensively explored hyperuniform states via SPV model by manipulating the cell perimeter elasticity K and the target shape index p_0 .

We observed hyperuniformity in both fluid and rigid tissue phases. In the fluid phase, surpassing the critical p_0^* consistently suppressed density fluctuations, evidenced by low hyperuniformity index H values and a distinct 'stealthy' hyperuniformity. In rigid phases, lowering K revealed that hyperuniform characteristics could be restored, emphasizing the crucial balance between perimeter and area constraints. This adaptability in the model offers valuable insights into cellu-

lar mechanics relevant to tissue development and disease understanding. The tunability of our model highlights its utility for simulating diverse tissue behaviors, beneficial for studying mechanical properties in realistic biological scenarios. Furthermore, these findings have profound implications for designing mechanical metamaterials, potentially inspiring new technologies that mimic the natural geometric and mechanical properties of tissues.

ACKNOWLEDGMENTS

We acknowledge support from the National Science Foundation (Grant Nos. DMR-2046683 and PHY-2019745), the National Institute of General Medical Sciences of the National Institutes of Health (Grant No. R35GM15049), the Alfred P. Sloan Foundation, and the Human Frontier Science Program (Reference No. RGP0007/2022).

METHODS

Simulating a confluent tissue monolayer To simulate the confluent tissue, N cells are randomly placed within a square box of size $L = \sqrt{N}$ under periodic boundary conditions. The average area per cell is unity. The default value for N is 2430 unless otherwise specified. Through the open-source software cellGPU [51], fast Inertial Relaxation Engine(FIRE) algorithm [45] is utilized to minimize the energy and obtain disordered ground states of the SPV model. We explore a range of perimeter modulus K values spanning from 0 to 1 and target shape index p_0 from 3.6 (solid) to 4.6 (liquid). A p_0 value of 4.6 corresponds to the perimeter of an equilateral triangle with unit area. In both cases with $K = 0$ and the rigid side of the transition, all structures undergo thorough minimization, ensuring that the maximum residual forces remain below 10^{-13} . While in the fluid side of the transition, minimization is challenging given the flat nature of the landscape. This challenge intensifies as the system delves deeper into the fluid states and with larger K values. Maximum force tolerances are adjusted accordingly. If the algorithm fails to reach the maximum force threshold, the simulation halts after reaching the maximum iteration limit 10^6 . Additionally, we examine the independence on the system size in Fig. S1 and the initial condition in Fig. S4.

Structure Factor The structure factor $S(\vec{q})$ is given by[52],

$$S(\vec{q}) = \frac{1}{N} \left\langle \sum_{j=1}^N \sum_{k=1}^N e^{-i\vec{q}(\vec{r}_j - \vec{r}_k)} \right\rangle \quad (2)$$

where \vec{r}_j is the position of j^{th} particle, and $\langle \cdot \rangle$ represents the ensemble average. $S(q)$ is the spherical average of $S(\vec{q})$ within reciprocal space at a radius q .

Effective Hyperuniformity Index It is a challenge to attain a rigorous statistical evaluation for hyperuniformity, largely due to the definition of the structure factor $S(q)$ at infinite

wavelength. Yet both numerical simulations and lab experiments encounter limitations from system size constraints and errors or noise inherent in measurements. To quantify these non-idealized samples how close to hyperuniformity, a hyperuniformity index H is raised,

$$H \equiv \frac{S(q \rightarrow 0)}{S(q_{\text{peak}})}, \quad (3)$$

where $S(q \rightarrow 0)$ is the estimated value of the structure factor at the origin and $S(q_{\text{peak}})$ is the value of the structure factor at the first dominant peak. An empirical criterion indicating "effective hyperuniformity" for a finite system is $H < 10^{-4}$ [24].

In the Voronoi model, there exists a subtle yet statistically significant nonmonotonic behavior in the structure factor at small wavenumbers, displaying either a plateau or a slight increase in the limit of large-length scales, as observed on a logarithmic scale. In previous approaches, the approximations of $S(q \rightarrow 0)$ have been made either by employing a linear extrapolation to $q = 0$ from a range excluding that nonmonotonic region[7] or by averaging the plateau [32]. Here we approximate the limiting behavior of $S(q \rightarrow 0)$ by taking the minimum value of $S(q)$, denoted as S_{min} . When the plateau is observed, S_{min} exhibits a similar value to the structure factor at the minimal $q = 2\pi/L$ or plateau range. Meanwhile, the value and reciprocal position of S_{min} demonstrate great robustness across various scaling regimes (Fig. S1) and initial states(Fig. S4). When the system size is not large enough to visualize the plateau, linear extrapolation might yield unreasonably small values. The closest approximation to the plateau average that we can obtain would be $S(q = 2\pi/L)$, which also is the minimum value of $S(q)$. This approach ensures that we can conveniently obtain H even in small systems. Once $H < 10^{-4}$ is achieved, we can confidently identify hyperuniform states, considering that H values may be overestimated compared to those obtained from larger systems.

Stealthy Hyperuniformity Stealthy hyperuniform patterns are a subclass of hyperuniform systems in which $S(q) = 0$ for $0 \leq q \leq q_{\text{th}}$. If S_{min} , i.e. the minimum value of $S(q)$, deviates from the reciprocal position of $2\pi/L$ without being limited by the system size, the system exhibits stealthy hyperuniformity[35]. The reciprocal position of S_{min} determines the threshold q_{th} and yields the associated χ in the thermodynamic limit, given by $q_{\text{th}}^2/(16\pi)$ [35]. χ measures the relative fraction of constrained degrees of freedom compared to the total number of degrees of freedom[18]. Remarkably, the finite-size effect observed in Fig. S1 reveals that stealthy hyperuniformity manifests not only in the rigid phase but also in the fluid phase, which may not be readily apparent in smaller systems.

Pair Correlation The pair correlation function is[53]

$$g(r) = \frac{1}{N\rho} \left\langle \sum_j \sum_{j \neq k} \delta(\vec{r} + \vec{r}_j - \vec{r}_k) \right\rangle \quad (4)$$

where ρ is the average particle density of the isotropic system, \vec{r}_j is the position of j^{th} particle, and $\langle \cdot \rangle$ represents the ensemble average.

Elastic moduli At the tissue level, its mechanical response is characterized by the shear modulus G . A non-zero G corresponds to a solid-like tissue while G vanishes for a fluid state. We obtain G by calculating the linear response to an infinitesimal affine strain γ via the Born-Huang formulation [54]

$$G = G_{\text{affine}} - G_{\text{non-affine}} = \frac{1}{A_{\text{total}}} \left[\frac{\partial^2 E}{\partial \gamma^2} - \Xi_{i\mu} M_{i\mu j\nu}^{-1} \Xi_{j\nu} \right]_{\gamma=0}. \quad (5)$$

In Eq. (5), $\Xi_{i\mu}$ is the derivative of the force on vertex i with respect to strain given by

$$\Xi_{i\mu} \equiv \frac{\partial^2 E}{\partial \gamma \partial r_{i\mu}}, \quad (6)$$

where $r_{i\mu}$ is the position of vertex i and $\mu = x, y$ is the Cartesian index. $A_{\text{total}} = \sum_i^N A_i$ is the total area of the tissue. M is the Hessian matrix given by the second derivative of the tissue energy E with respect to position vectors of vertices i and j

$$M_{i\mu j\nu} = \frac{\partial^2 E}{\partial r_{i\mu} \partial r_{j\nu}}. \quad (7)$$

To calculate the bulk modulus, we consider the isotropic compression process, $x \rightarrow x' = \lambda x$, $y \rightarrow y' = \lambda y$. Here λ is compressional ratio along x and y directions. So the strain tensor is defined by

$$\begin{pmatrix} \gamma_{xx} & \gamma_{xy} \\ \gamma_{yx} & \gamma_{yy} \end{pmatrix} = \begin{pmatrix} \lambda - 1 & 0 \\ 0 & \lambda - 1 \end{pmatrix} \quad (8)$$

Similar to the shear modulus G , we also calculate the bulk modulus using the linear response to an infinitesimal strain tensor.

$$\begin{aligned} B &= B_{\text{affine}} - B_{\text{non-affine}} \\ &= \frac{1}{2A_{\text{total}}} \left\{ \left[\frac{\partial^2 E}{\partial \gamma_{xx}^2} - \Xi_{i\mu} M_{i\mu j\nu}^{-1} \Xi_{j\nu} \right]_{\gamma_{xx}=0} \right. \\ &\quad \left. + \left[\frac{\partial^2 E}{\partial \gamma_{yy}^2} - \Xi_{i\mu} M_{i\mu j\nu}^{-1} \Xi_{j\nu} \right]_{\gamma_{yy}=0} \right\} \quad (9) \end{aligned}$$

Because $\gamma_{xx} = \lambda - 1$, the derivation of E with respect to γ_{xx} would be the same with that of λ at the limit $\lambda \rightarrow 1$. Finally, we have the bulk modulus

$$\begin{aligned} B &= B_{\text{affine}} - B_{\text{non-affine}} \\ &= \frac{1}{2A_{\text{total}}} \left\{ \left[\frac{\partial^2 E}{\partial \lambda^2} - \Xi_{i\mu} M_{i\mu j\nu}^{-1} \Xi_{j\nu} \right]_{\lambda=1} \right. \\ &\quad \left. + \left[\frac{\partial^2 E}{\partial \eta^2} - \Xi_{i\mu} M_{i\mu j\nu}^{-1} \Xi_{j\nu} \right]_{\eta=1} \right\} \quad (10) \end{aligned}$$

* Corresponding author: d.bi@northeastern.edu

- [1] David J Vezzetti. A new derivation of some fluctuation theorems in statistical mechanics. *Journal of Mathematical Physics*, 16(1):31–33, 1975.
- [2] Robert M Ziff. On the bulk distribution functions and fluctuation theorems. *Journal of Mathematical Physics*, 18(9):1825–1831, 1977.
- [3] Yang Jiao, Hal Berman, Tim-Rasmus Kiehl, and Salvatore Torquato. Spatial organization and correlations of cell nuclei in brain tumors. *PLOS ONE*, 6(11):e27323, 2011.
- [4] Adam Wax, Changhui Yang, Vadim Backman, Kamran Badizadegan, Charles W. Boone, Ramachandra R. Dasari, and Michael S. Feld. Cellular organization and substructure measured using angle-resolved low-coherence interferometry. *Biophysical Journal*, 82(4):2256–2264, April 2002.
- [5] Salvatore Torquato and Frank H. Stillinger. Local density fluctuations, hyperuniformity, and order metrics. *Phys. Rev. E*, 68(4):041113, October 2003.
- [6] Salvatore Torquato. Hyperuniform states of matter. *Physics Reports*, 745:1–95, June 2018.
- [7] Michael A. Klatt, Jakov Lovrić, Duyu Chen, Sebastian C. Kapfer, Fabian M. Schaller, Philipp W. A. Schönhöfer, Bruce S. Gardiner, Ana-Sunčana Smith, Gerd E. Schröder-Turk, and Salvatore Torquato. Universal hidden order in amorphous cellular geometries. *Nat Commun*, 10(1):811, February 2019.
- [8] Olivier Leseur, Romain Pierrat, and Rémi Carminati. High-density hyperuniform materials can be transparent. *Optica*, 3(7):763–767, 2016.
- [9] Marian Florescu, Salvatore Torquato, and Paul J Steinhardt. Designer disordered materials with large, complete photonic band gaps. *Proceedings of the National Academy of Sciences*, 106(49):20658–20663, 2009.
- [10] Xinzhi Li, Amit Das, and Dapeng Bi. Biological tissue-inspired tunable photonic fluid. *Proceedings of the National Academy of Sciences*, 115(26):6650–6655, June 2018.
- [11] Luis S Froufe-Pérez, Michael Engel, Pablo F Damasceno, Nicolas Muller, Jakub Haberkov, Sharon C Glotzer, and Frank Scheffold. Role of short-range order and hyperuniformity in the formation of band gaps in disordered photonic materials. *Physical review letters*, 117(5):053902, 2016.
- [12] Yaopengxiao Xu, Shaohua Chen, Pei-En Chen, Wenxiang Xu, and Yang Jiao. Microstructure and mechanical properties of hyperuniform heterogeneous materials. *Physical Review E*, 96(4):043301, 2017.
- [13] Duyu Chen and Salvatore Torquato. Designing disordered hyperuniform two-phase materials with novel physical properties. *Acta Materialia*, 142:152–161, 2018.
- [14] S Torquato. Modeling of physical properties of composite materials. *International Journal of Solids and Structures*, 37(1-2):411–422, 2000.
- [15] Ge Zhang, Frank H Stillinger, and Salvatore Torquato. The perfect glass paradigm: Disordered hyperuniform glasses down to absolute zero. *Scientific reports*, 6(1):36963, 2016.
- [16] Georgios Gkantzounis, Timothy Amoah, and Marian Florescu. Hyperuniform disordered phononic structures. *Physical Review B*, 95(9):094120, 2017.
- [17] Elie Chéron, Jean-Philippe Groby, Vincent Pagneux, Simon Félix, and Vicent Romero-García. Experimental characterization of rigid-scatterer hyperuniform distributions for audible acoustics. *Physical Review B*, 106(6):064206, 2022.
- [18] Robert D. Batten, Frank H. Stillinger, and Salvatore Torquato. Classical disordered ground states: Super-ideal gases and stealth and equi-luminous materials. *J. Appl. Phys.*, 104(3), August 2008.
- [19] G. Zhang, F. H. Stillinger, and S. Torquato. Ground states of

- stealthy hyperuniform potentials: I. entropically favored configurations. *Phys. Rev. E*, 92(2):022119, August 2015.
- [20] Obioma U. Uche, Frank H. Stillinger, and Salvatore Torquato. Constraints on collective density variables: Two dimensions. *Phys. Rev. E*, 70(4):046122, October 2004.
- [21] Peter K. Morse, Jaeuk Kim, Paul J. Steinhardt, and Salvatore Torquato. Generating large disordered stealthy hyperuniform systems with ultrahigh accuracy to determine their physical properties. *Phys. Rev. Res.*, 5(3):033190, September 2023.
- [22] Qiang Du, Vance Faber, and Max Gunzburger. Centroidal voronoi tessellations: Applications and algorithms. *SIAM review*, 41(4):637–676, 1999.
- [23] Arman Boromand, Alexandra Signoriello, Fangfu Ye, Corey S O’Hern, and Mark D Shattuck. Jamming of deformable polygons. *Physical review letters*, 121(24):248003, 2018.
- [24] Steven Atkinson, Ge Zhang, Adam B. Hopkins, and Salvatore Torquato. Critical slowing down and hyperuniformity on approach to jamming. *Phys. Rev. E*, 94(1):012902, July 2016.
- [25] Lior Atia, Dapeng Bi, Yasha Sharma, Jennifer A. Mitchel, Bomi Gweon, Stephan A. Koehler, Stephen J. DeCamp, Bo Lan, Jae Hun Kim, Rebecca Hirsch, Adrian F. Pegoraro, Kyu Ha Lee, Jacqueline R. Starr, David A. Weitz, Adam C. Martin, Jin-Ah Park, James P. Butler, and Jeffrey J. Fredberg. Geometric constraints during epithelial jamming. *Nature Phys.*, 14(6):613–620, June 2018.
- [26] Dapeng Bi, Xingbo Yang, M. Cristina Marchetti, and M. Lisa Manning. Motility-driven glass and jamming transitions in biological tissues. *Physical Review X*, 6(2):021011, April 2016.
- [27] Simon Garcia, Edouard Hannezo, Jens Elgeti, Jean-François Joanny, Pascal Silberzan, and Nir S. Gov. Physics of active jamming during collective cellular motion in a monolayer. *Proceedings of the National Academy of Sciences*, 112(50):15314–15319, December 2015.
- [28] Wenying Kang, Jacopo Ferruzzi, Catalina-Paula Spatarelu, Yu Long Han, Yasha Sharma, Stephan A. Koehler, Jennifer A. Mitchel, Adil Khan, James P. Butler, Darren Roblyer, Muhammad H. Zaman, Jin-Ah Park, Ming Guo, Zi Chen, Adrian F. Pegoraro, and Jeffrey J. Fredberg. A novel jamming phase diagram links tumor invasion to non-equilibrium phase separation. *iScience*, 24(11):103252, November 2021.
- [29] Jennifer A. Mitchel, Amit Das, Michael J. O’Sullivan, Ian T. Stancil, Stephen J. DeCamp, Stephan Koehler, Oscar H. Ocaña, James P. Butler, Jeffrey J. Fredberg, M. Angela Nieto, Dapeng Bi, and Jin-Ah Park. In primary airway epithelial cells, the unjamming transition is distinct from the epithelial-to-mesenchymal transition. *Nat Commun.*, 11(1):5053, December 2020.
- [30] Jennifer A. Mitchel, Amit Das, Michael J. O’Sullivan, Ian T. Stancil, Stephen J. DeCamp, Stephan Koehler, James P. Butler, Jeffrey J. Fredberg, M. Angela Nieto, Dapeng Bi, and Jin-Ah Park. The unjamming transition is distinct from the epithelial-to-mesenchymal transition. Preprint, Biophysics, June 2019.
- [31] Alessandro Mongera, Payam Rowghanian, Hannah J. Gustafson, Elijah Shelton, David A. Kealhofer, Emmet K. Carn, Friedhelm Serwane, Adam A. Lucio, James Giammona, and Otger Campàs. A fluid-to-solid jamming transition underlies vertebrate body axis elongation. *Nature*, 561(7723):401–405, September 2018.
- [32] Yuanjian Zheng, Yan-Wei Li, and Massimo Pica Ciamarra. Hyperuniformity and density fluctuations at a rigidity transition in a model of biological tissues. *Soft Matter*, 16(25):5942–5950, July 2020.
- [33] Yang Jiao, Timothy Lau, Haralampos Hatzikirou, Michael Meyer-Hermann, Joseph C. Corbo, and Salvatore Torquato. Avian photoreceptor patterns represent a disordered hyperuniform solution to a multiscale packing problem. *Phys. Rev. E*, 89(2):022721, February 2014.
- [34] Yuan Liu, Duyu Chen, Jianxiang Tian, Wenxiang Xu, and Yang Jiao. Universal hyperuniform organization in looped leaf vein networks. *Physical Review Letters*, 133(2):028401, 2024.
- [35] S. Torquato, G. Zhang, and F. H. Stillinger. Ensemble theory for stealthy hyperuniform disordered ground states. *Phys. Rev. X*, 5(2):021020, May 2015.
- [36] Reza Farhadifar, Jens-Christian Röper, Benoit Aigouy, Suzanne Eaton, and Frank Jülicher. The influence of cell mechanics, cell-cell interactions, and proliferation on epithelial packing. *Current Biology*, 17(24):2095–2104, December 2007.
- [37] Jin-Ah Park, Jae Hun Kim, Dapeng Bi, Jennifer A. Mitchel, Nader Taheri Qazvini, Kelan Tantisira, Chan Young Park, Maureen McGill, Sae-Hoon Kim, Bomi Gweon, Jacob Notbohm, Robert Steward Jr, Stephanie Burger, Scott H. Randell, Alvin T. Kho, Dhananjay T. Tambe, Corey Hardin, Stephanie A. Shore, Elliot Israel, David A. Weitz, Daniel J. Tschumperlin, Elizabeth P. Henske, Scott T. Weiss, M. Lisa Manning, James P. Butler, Jeffrey M. Drazen, and Jeffrey J. Fredberg. Unjamming and cell shape in the asthmatic airway epithelium. *Nature Mater.*, 14(10):1040–1048, October 2015.
- [38] G. Lejeune Dirichlet. Über die reduction der positiven quadratischen formen mit drei unbestimmten ganzen zahlen. *Journal für die reine und angewandte Mathematik (Crelles Journal)*, 1850(40):209–227, July 1850.
- [39] Hisao Honda. Description of cellular patterns by dirichlet domains: The two-dimensional case. *Journal of Theoretical Biology*, 72(3):523–543, June 1978.
- [40] D. B. Staple, R. Farhadifar, J. C. Röper, B. Aigouy, S. Eaton, and F. Jülicher. Mechanics and remodelling of cell packings in epithelia. *Eur. Phys. J. E*, 33(2):117–127, October 2010.
- [41] Lars Hufnagel, Aurelio A. Teleman, Hervé Rouault, Stephen M. Cohen, and Boris I. Shraiman. On the mechanism of wing size determination in fly development. *Proceedings of the National Academy of Sciences*, 104(10):3835–3840, March 2007.
- [42] Steven M. Zehnder, Melanie Suaris, Madison Claire M. Bellaire, and Thomas E. Angelini. Cell volume fluctuations in mdck monolayers. *Biophys J.*, 108(2):247–250, January 2015.
- [43] Dapeng Bi, J. H. Lopez, J. M. Schwarz, and M. Lisa Manning. A density-independent rigidity transition in biological tissues. *Nature Phys.*, 11(12):1074–1079, December 2015.
- [44] Erik Bitzek, Pekka Koskinen, Franz Gähler, Michael Moseler, and Peter Gumbsch. Structural relaxation made simple. *Phys. Rev. Lett.*, 97:170201, Oct 2006.
- [45] Julien Guérolé, Wolfram G. Nöhring, Aviral Vaid, Frédéric Houllé, Zhuocheng Xie, Aruna Prakash, and Erik Bitzek. Assessment and optimization of the fast inertial relaxation engine (fire) for energy minimization in atomistic simulations and its implementation in lammps. *Computational Materials Science*, 175:109584, April 2020.
- [46] A. Gabrielli, M. Joyce, and S. Torquato. Tilings of space and superhomogeneous point processes. *Phys. Rev. E*, 77(3):031125, March 2008.
- [47] MJ Godfrey and MA Moore. Absence of hyperuniformity in amorphous hard-sphere packings of nonvanishing complexity. *Physical Review Letters*, 121(7):075503, 2018.
- [48] Joaquín Puig, Federico Elías, Jazmín Aragón Sánchez, Raúl Cortés Maldonado, Gonzalo Rumi, Gladys Nieva, Pablo Pedrazzini, Alejandro B Kolton, and Yanina Fasano. Anisotropic suppression of hyperuniformity of elastic systems in media with planar disorder. *Communications Materials*, 3(1):32, 2022.

- [49] Le Yan and Dapeng Bi. Multicellular rosettes drive fluid-solid transition in epithelial tissues. Phys. Rev. X, 9(1):011029, February 2019.
- [50] Marjolein Dijkstra and Robert Evans. A simulation study of the decay of the pair correlation function in simple fluids. The Journal of Chemical Physics, 112(3):1449–1456, 2000.
- [51] Daniel M. Sussman. cellgpu: Massively parallel simulations of dynamic vertex models. Computer Physics Communications, 219:400–406, October 2017.
- [52] JP Hansen and IR McDonald. Chapter 4-distribution function theories, in theory of simple liquids, 2013.
- [53] JP Hansen and IR McDonald. Chapter 2-statistical mechanics., in theory of simple liquids, 2013.
- [54] Craig E. Maloney and Anaël Lemaître. Amorphous systems in athermal, quasistatic shear. Phys. Rev. E, 74:016118, Jul 2006.

SUPPLEMENTAL FIGURES

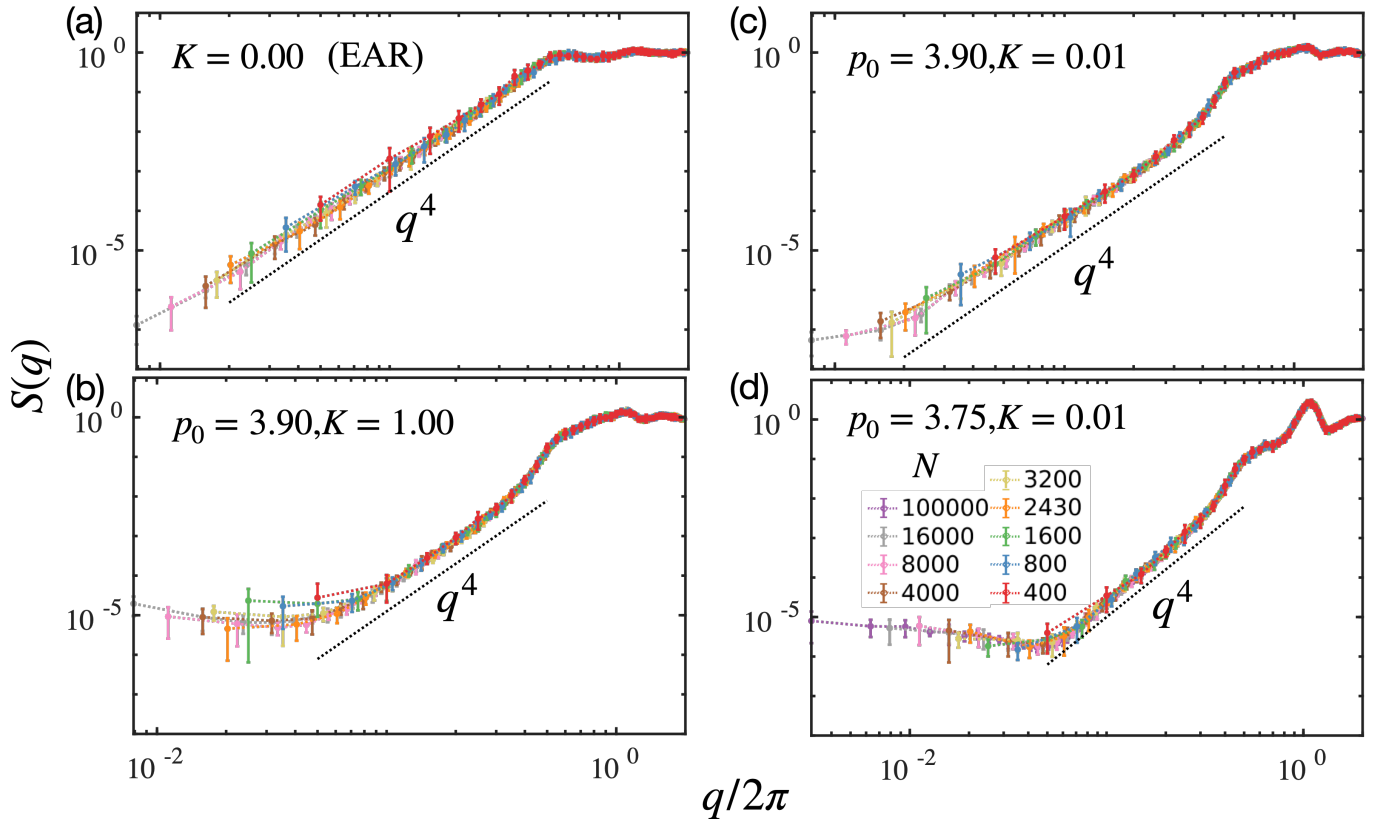


Fig. S1. **The finite-size effect for structure factor in different hyperuniformity systems** The shape of the structure factor $S(q)$ is independent of the system sizes. (a) The diminishing trend of the structure factor persists within the EAR packing as q decreases, without leveling off, suggesting strict hyperuniformity. It is well fitted by $S(q) \sim (q/2\pi)^4$. (b) With larger N , the structure factor unveils a plateau in the small q range, effectively showcasing the manifestation of stealthy hyperuniformity within tissues in fluid states. (c) The reduction of K from 1 to 0.01 drives $S(q)$ to continue decreasing at small q range, with the plateau expected to occur at smaller q_{th} values and with lower magnitude. (b,d) The stability of q_{th} and its corresponding S_{min} supports the methods for calculating effective hyperuniformity index H .

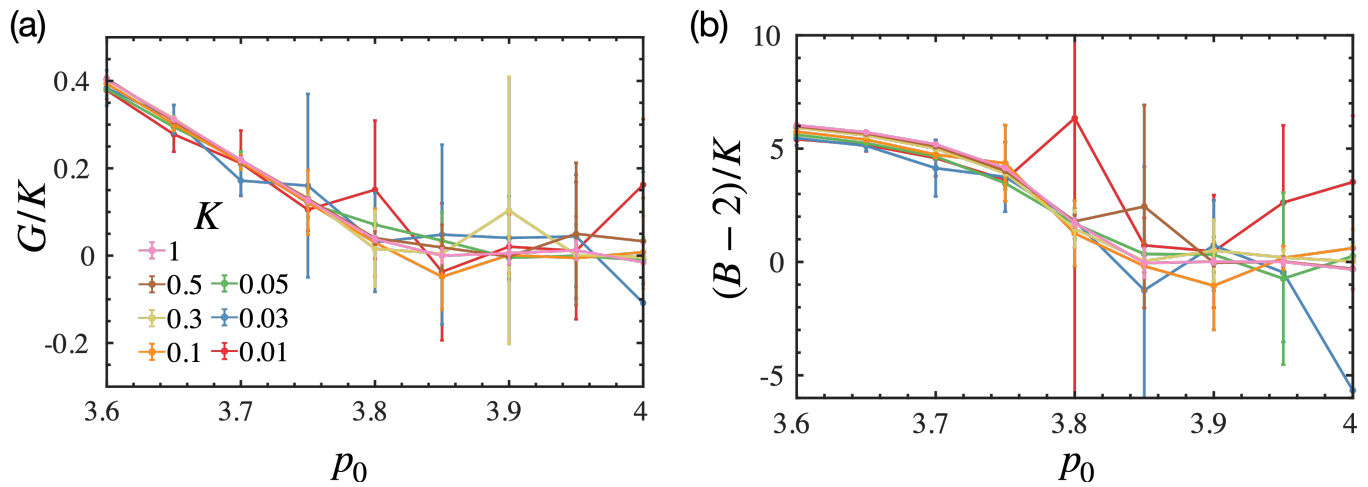


Fig. S2. **Elastic moduli characterize the tissue's rigidity** (a) The rescaled shear modulus G/K and (b) the rescaled bulk modulus $(B-2)/K$ as the function of p_0 for various K collapse onto a polyline. As p_0 increases, the tissues become less rigid. Both the shear modulus G and the bulk modulus B decrease, with the rate of increase being linear with respect to K . Ultimately, the tissues transit into the fluid phase, featured by vanished shear modulus $G = 0$, and constant bulk modulus $B = 2$.

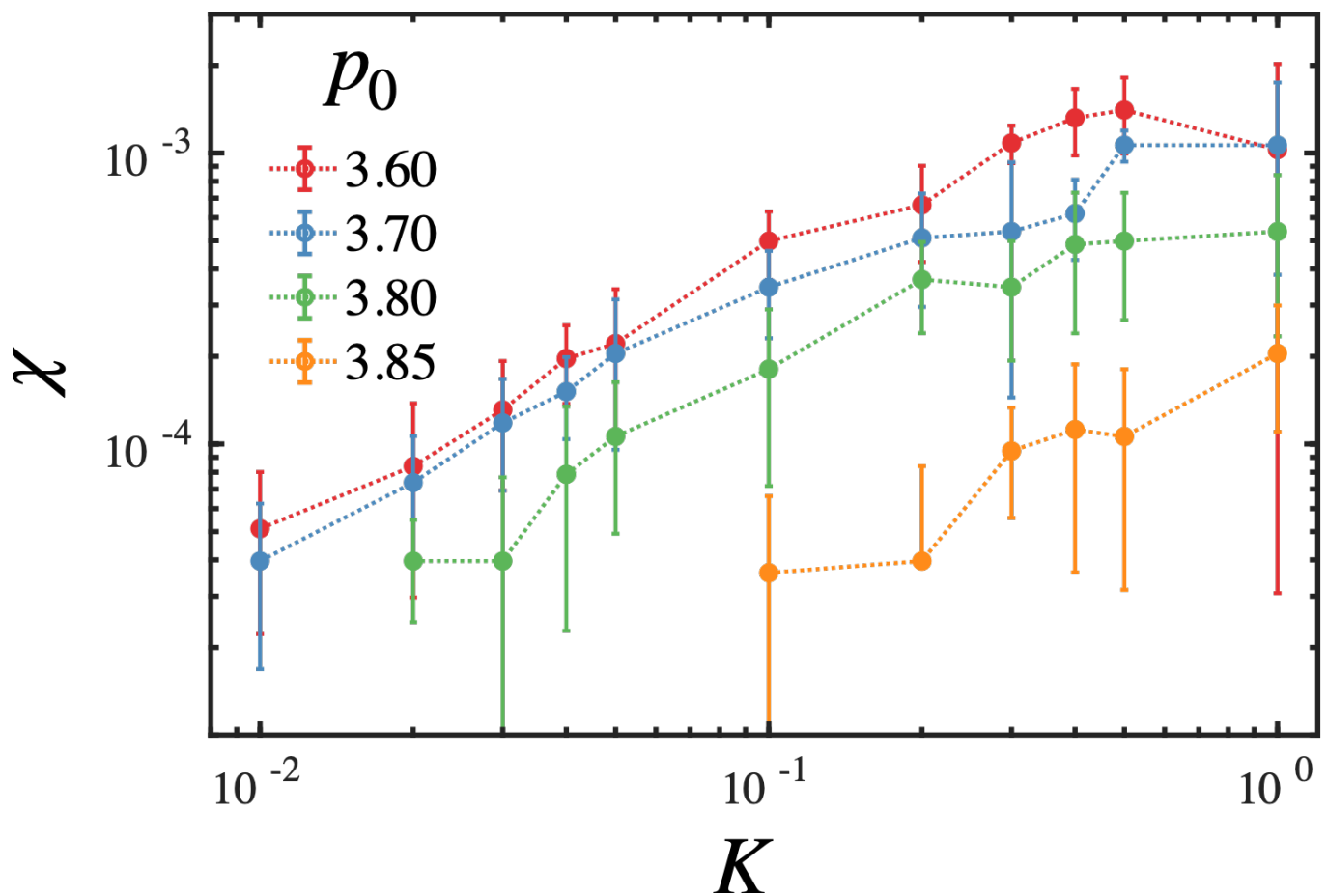


Fig. S3. **Down-regulating K decreases stealthiness parameter χ of hyperuniformity.** The χ values are obtained from $N = 2430$ cell system and plotted in log-log scale.

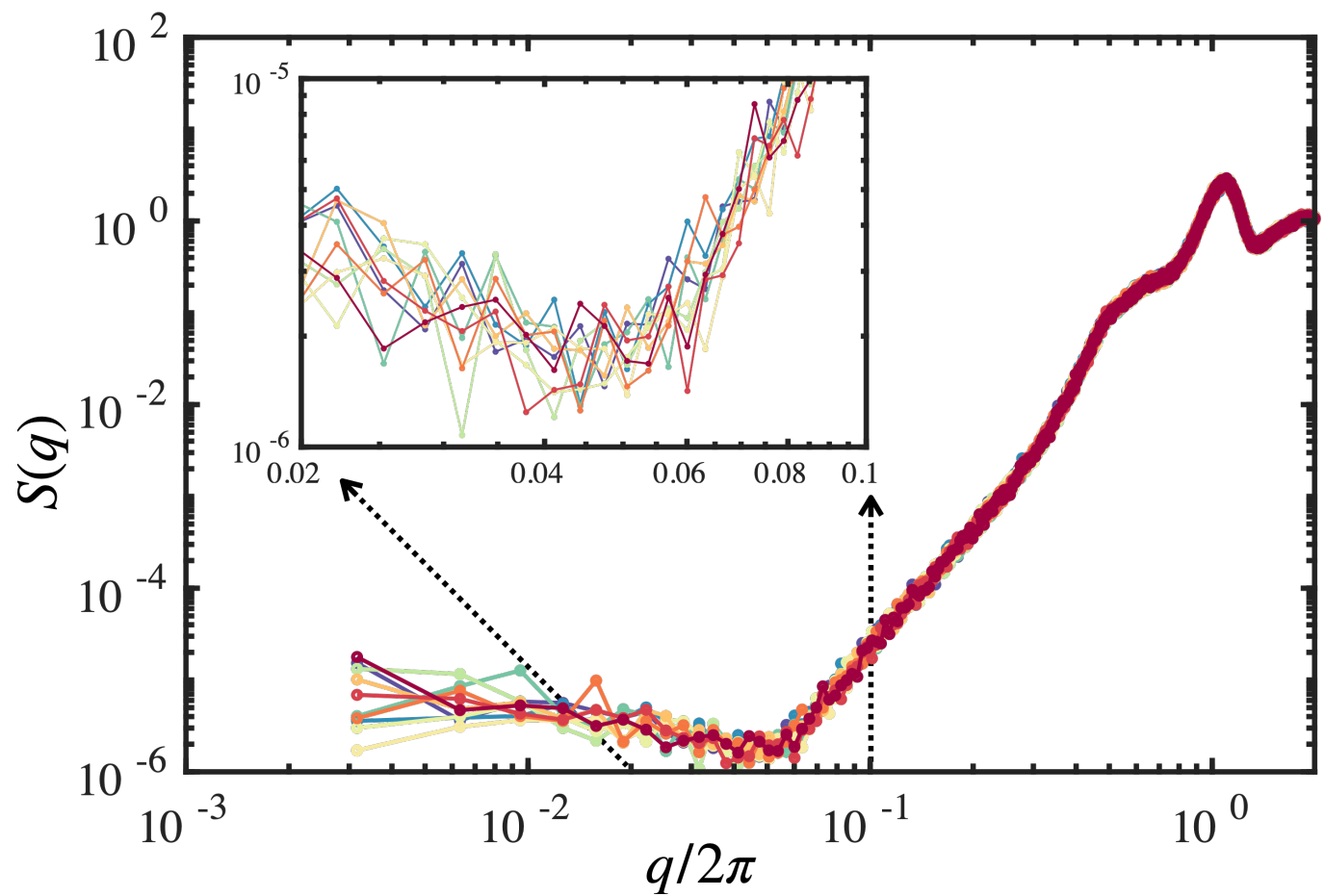


Fig. S4. **Structure factor for various random initial configurations.** The value of S_{min} exhibits greater robustness compared to $S(2\pi/L)$, as does the location q_{th} . These findings enhance the credibility of the approximation of effective hyperuniformity index H .

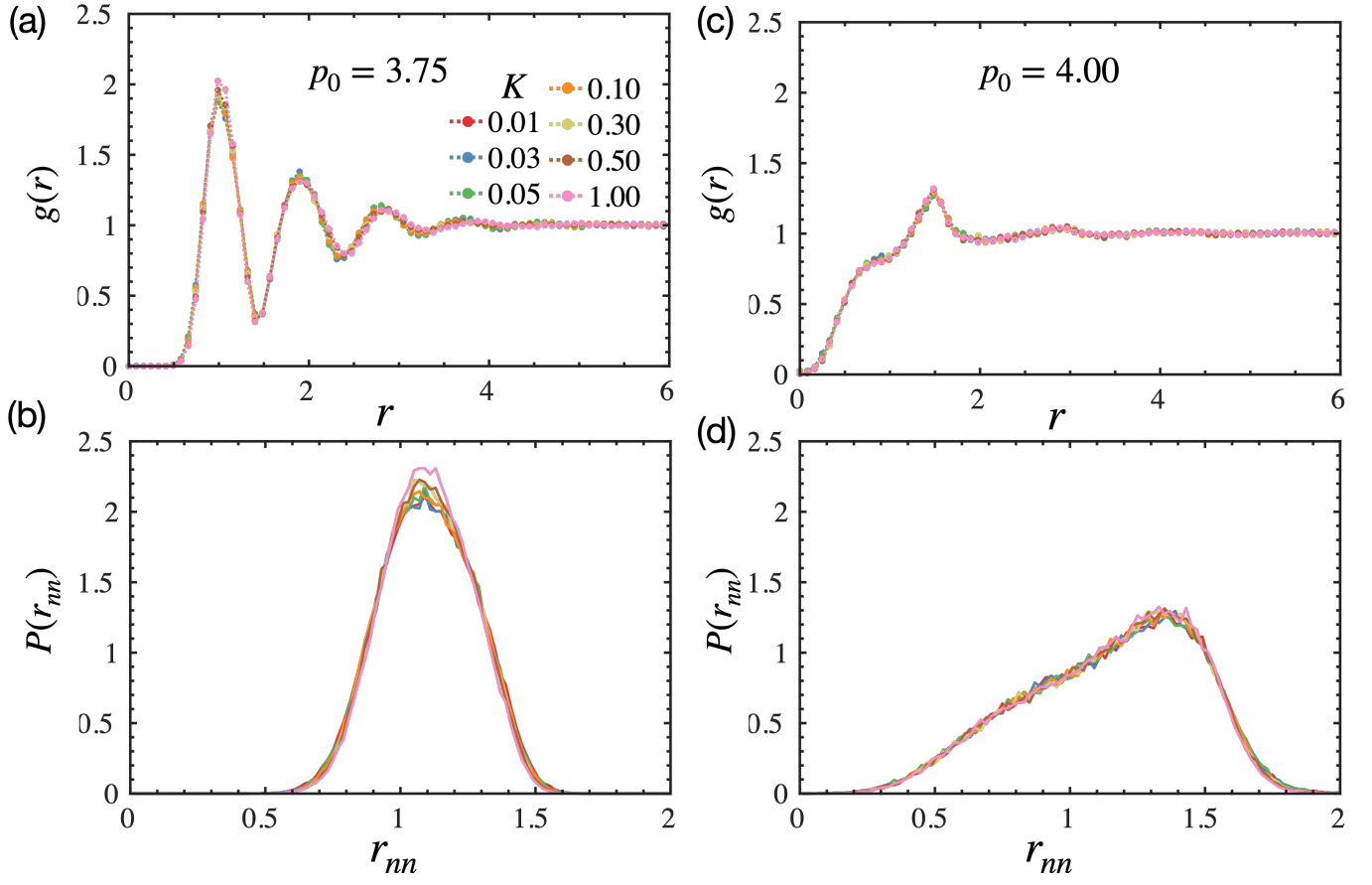


Fig. S5. **Perimeter elasticity does not affect the short-range order.** In both (a,b) the solid phase and (c,d) the fluid phase, (a,c) the pair correlation function $g(r)$ and (b,d) the probability density function of the distance between neighboring cells r_{nn} are near identical across various values of perimeter elasticity K .

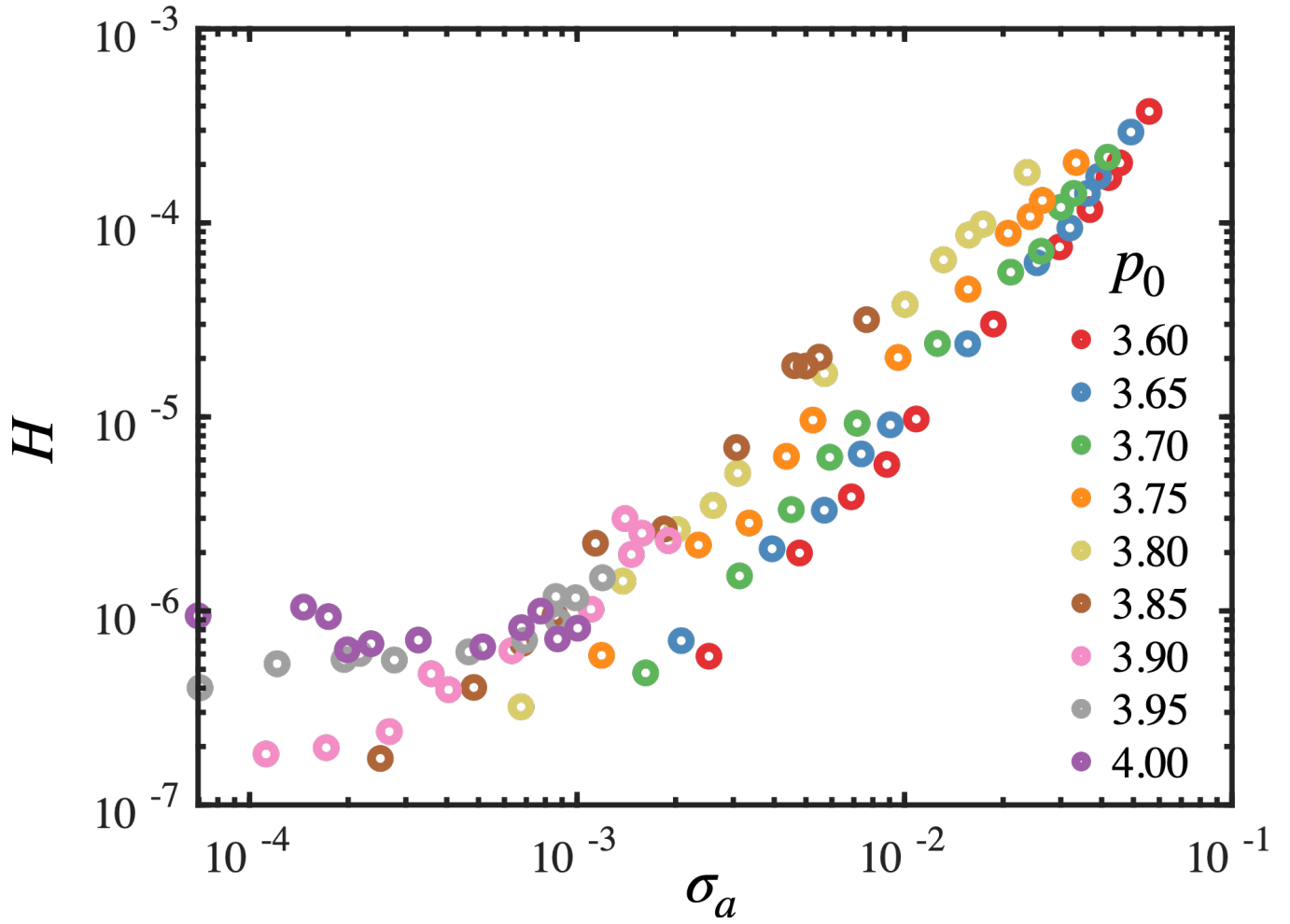


Fig. S6. **Area fluctuation σ_a effectively characterizes the hyperuniformity.** σ_a presents a positive correlation with hyperuniformity index H across various p_0 . When $\sigma_a > 10^{-3}$, H increases with increased σ_a .